

Quantum-mechanical understanding on structure dependence of image potentials of single-walled boron nitride nanotubes

Yu Zhang(张煜), Zhiman Zhang(张芷蔓), Weiliang Wang(王伟良), Shaolin Zhang(张绍林), and Haiming Huang(黄海鸣)

Citation: Chin. Phys. B, 2024, 33 (**12**): 128501. DOI: 10.1088/1674-1056/ad8071
Journal homepage: http://cpb.iphy.ac.cn; http://iopscience.iop.org/cpb

What follows is a list of articles you may be interested in

Design and optimization of a nano-antenna hybrid structure for solar energy harvesting application

Mohammad Javad Rabienejhad, Mahdi Davoudi-Darareh, and Azardokht Mazaheri
Chin. Phys. B, 2021, 30 (**9**): 098503. DOI: 10.1088/1674-1056/abea8e

Vibration and buckling analyses of nanobeams embedded in an elastic medium

S Chakraverty, Laxmi Behera
Chin. Phys. B, 2015, 24 (**9**): 097305. DOI: 10.1088/1674-1056/24/9/097305

Dependence of the electrical properties of defective single-walled carbon nanotubes on the vacancy density

Luo Yu-Pin(罗煜聘), Tien Li-Gan(田力耕), Tsai Chuen-Horng(蔡春鸿), Lee Ming-Hsien(李明宪), and Li Feng-Yin(李丰颖)
Chin. Phys. B, 2011, 20 (**8**): 087303. DOI: 10.1088/1674-1056/20/8/087303

Quantum-mechanical understanding on structure dependence of image potentials of single-walled boron nitride nanotubes

Yu Zhang(张煜)[1,2,†], Zhiman Zhang(张芷蔓)[1,†], Weiliang Wang(王伟良)[3], Shaolin Zhang(张绍林)[1,2], and Haiming Huang(黄海鸣)[1,2,‡]

[1] *Solid State Physics & Material Research Laboratory, School of Physics and Materials Science, Guangzhou University, Guangzhou* 510006, *China*
[2] *Research Center for Advanced Information Materials (CAIM), Huangpu Research and Graduate School of Guangzhou University, Guangzhou* 510555, *China*
[3] *School of Physics, Guangdong Province Key Laboratory of Display Material and Technology, Center for Neutron Science and Technology, Sun Yat-sen University, Guangzhou* 510275, *China*

(Received 18 July 2024; revised manuscript received 25 September 2024; accepted manuscript online 27 September 2024)

The recent discovery of field emission devices based on one-dimensional nanostructures has attracted much interest in emerging applications on next-generation flat panel displays, molecule-based sensors, and so forth. To achieve a comprehensive understanding of surface potentials at the nano-emitters during the tunneling process, in this study we systematically investigated the image potentials of single-walled boron nitride nanotubes with different edges, diameters and lengths in the frame of a composite first-principles calculation. The image potentials of zigzag single-walled boron nitride nanotubes are found to be dependent on the non-equivalent sides. Only the image potentials of isolated armchair single-walled boron nitride nanotube can be well fitted with the image potential of an ideal metal sphere of a size comparable to the tube diameter. On the contrary, the image potentials of zigzag and grounded armchair single-walled boron nitride nanotubes exhibit a strong length-dependence characteristic and are significantly different from that of an ideal metal sphere, which originates from the significant axial symmetry breaking of induced charge at the tip for the long tube. The correlation between the testing electron and electronic structure of single-walled boron nitride nanotube has also been discussed.

Keywords: boron nitride nanotubes, quantum chemistry, image potentials, structure dependence

PACS: 85.45.Db, 73.63.Fg, 73.22.–f, 85.30.Hi **DOI:** 10.1088/1674-1056/ad8071

1. Introduction

Field emission (FE) is a quantum tunneling effect of electrons escaping from the surface potential barrier of a material under an external electric field,[1] which is becoming the focus of technological tools to investigate the electron source morphology[2,3] and surface/interface properties of micro-nano structure[4–7] owing to its ultra-fast response time, low-voltage operation, and avoidance of high-temperature heating. Cold electron emitters with excellent field emission features are demanded in many vacuum electronic applications (e.g., flat panel displays,[8,9] parallel e-beam lithography systems[10–12] and light-emitting diodes[13–15]) to enhance the reliability performance. To date, more than a dozen electron-emitting materials, including metal oxides,[16–18] silicon carbides[19,20] and transition metal carbides,[21–23] have been studied. However, critical obstacles to the real application of an emitter, including the gaseous pollutants in the industrial conditions[24–26] and morphologic changes during the secondary processes,[27–29] still should be overcome. One-dimensional (1D) nanomaterials, such as carbon nanotubes (CNTs) and boron nitride nanotubes (BNNTs), have been observed to exhibit outstanding field emission properties due to the extremely strong local fields and high current densities caused by the very high aspect ratios.[30,31] Particularly, BNNTs are considered to be promising materials for cold electron emission because of their high negative electron affinity[32] and excellent oxidation resistance.[33] Relevant studies have demonstrated that synthesized BNNTs exhibit remarkable FE performance, such as high current densities,[34] endurance under harsh ambient conditions[35] and long-term emission stability.[36] However, compared with the previous abundant studies of BNNTs from an experimental viewpoint, up to now complementary computational efforts to understand the electronic properties and potential barriers at the emitting surface during the FE process are still lacking.

Image potential caused by electrons situated at a finite distance from the tip of an emitter is one of the most important technological parameters of the FE process since it would reduce the barrier height of the electron on the vacuum side of the vacuum–emitter interface and thus enhance electron tunneling probability significantly,[37] making the FE process easier.[38,39] However, the image potential of nanoscale emitter remains incompletely understood.[40] The image potential of the ideal metal plane model adopted by classical Fowler–Nordheim law is found to be no longer valid for atomic sharp emitter.[41–43] Previous studies[44] have indicated that the image potentials of single-walled CNTs are insensitive to the ap-

[†]These authors contributed equally to this work.
[‡]Corresponding author. E-mail: huanghm@gzhu.edu.cn
© 2024 Chinese Physical Society and IOP Publishing Ltd

plied fields and structures in FE conditions. By using the composite quantum chemistry method, the image potential of C_{60} is found to be isotropic and independent of temperature.[45] In addition, the image potential of the nanoscale system has been predicted to be affected by charge redistribution, leading to significant alterations in energy levels and the induction of image states on material surfaces.[46–48] Using combined LDA + image potential calculations, the image-potential states of graphene have been predicted to present potential applications in the investigation of the effects of the topography, intersheet and impurity interactions on spectroscopic and dynamical properties.[49,50] By combining the scanning tunneling microscopy and spectroscopy techniques,[51–53] the surface's image potential states of materials[54,55] have been successfully probed on clean metal surfaces and found to be closely matched with the theoretical model of self-energy formalism based on the many-body theory.[56–58] More recent investigations not only extended the theoretical models to two-dimensional nanomaterials (e.g., graphene,[59,60] germanene,[61] and borophene[62,63]), but also emphasized the substrate effects in electron transfer processes. However, a limited number of studies have been conducted on the image potentials of BNNTs. How the length, diameter and chirality of BNNT affect the electronic structure, charge distribution and surface potential remains unclarified. Furthermore, the interplay between the testing electron and electronic structures of BNNTs needs to be studied in depth.

To clarify the above issues, a comprehensive quantum mechanical investigation has been performed in the present paper to understand the detailed electronic structure of single-walled boron nitride nanotubes (SWBNNTs), especially the charge distribution and the potential barrier in the tip region. We calculated the image potentials of SWBNNTs with various chiral indices, lengths and diameters under both isolated and grounded conditions. A detailed description of the computational methodology is provided in Section 2, while Section 3 presents the computed results and the corresponding discussion. Conclusions are given in Section 4.

2. Calculation method

In the present work, using the general atomic and molecular electronic structure system (GAMESS),[64] we employed density functional theory (DFT) with the B3LYP hybrid functional[65,66] to investigate the electronic properties[67] and image potentials of SWBNNTs. All dangling bonds at the artificial open edge were saturated by hydrogen atoms.[68] As examples of structures of the hydrogen-saturated SWBNNTs, the models of zigzag-edge SWBNNT (Z-SWBNNT) and armchair-edge SWBNNT (A-SWBNNT) are illustrated in Fig. 1. For convenience, the SWBNNTs are defined as (N, M, L), where integers N and M that are not less than zero are chirality indices while L represents the number of repeating units along the tube axis. As shown in Fig. 1, a Z-SWBNNT (A-SWBNNT) corresponds to the case of $N > M = 0$ ($N = M$). The structure details of the considered SWBNNTs, including the number of atoms, the total number of electrons, diameter, and length, are provided in Table S1 of the supplementary file. To investigate the potential barriers of SWBNNTs, non-equivalent emitting points I, II, III, and VI (V, VI and VII) for Z-SWBNNT (A-SWBNNT) have been considered, as indicated by arrows in Fig. 1. The distance z between the testing electron and the emitter is defined as the distance along the two red line segments, as shown in Fig. 1. Particularly, due to the presence of non-equivalence terminations (i.e., H–B and H–N side) for Z-SWBNNTs, both sides need to be taken into account.

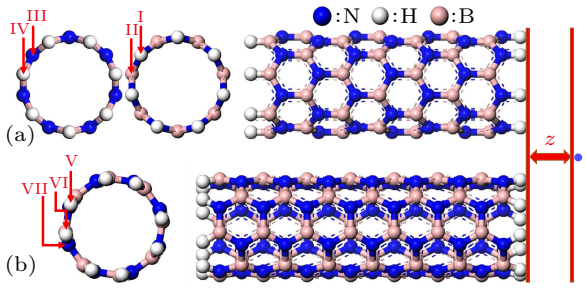


Fig. 1. (a) Schematic illustration of a testing electron near the tip of (7, 0, 3) Z-SWBNNT. The left, middle and right subgraphs represent the front view of the H–B side, the front view of the H–N side and the side view, respectively. (b) Schematic illustration of a testing electron near the tip of (4, 4, 5) A-SWBNNT. The left (right) panel represents the front (side) view. The non-equivalent emitting points are indicated by arrows. The distance between the SWBNNTs and the testing electron is defined as z.

To explore the image potentials of SWBNNTs, isolated and grounded SWBNNT in equilibrium state have been considered to be in the canonical and grand canonical ensembles, respectively, and the Fermi level of the substrate has been set to -5 eV throughout the nanotube for the latter case. To obtain the potential barrier, we moved a testing electron along a line from the emitting point to a remote location far away from the tip and calculated the electric force on the testing electron along this path. The electric force on the testing electron can be straightforwardly calculated by DFT for isolated cases since only the electron distribution of the SWBNNT in the Coulomb potential of the testing electron will be changed, meeting the variational constraint of DFT. On the other hand, according to the grand canonical ensemble, due to the electron and energy exchange between the SWBNNT and the substrate for the grounded case, the macroscopic electric field $\bar{E}(z)$ at the position z of the testing electron should be uniquely determined by weighted average

$$\bar{E}(z) = \sum_{N_e,s} \rho_{N_e,s} E_{N_e,s}, \tag{1}$$

where $\rho_{N_e,s}$ and $E_{N_e,s}(z)$ represent the probability and electric field of grounded SWBNNT in a quantum state with electron

number N_e and energy $U_{N_e,s}$, respectively. $\rho_{N_e,s}$ is given by

$$\rho_{N_e,s} = \frac{\exp(-\alpha N_e - \beta U_{N_e,s})}{\sum_{N_e,s} \exp(-\alpha N_e - \beta U_{N_e,s})}. \quad (2)$$

Particularly, $\alpha = -\mu/(k_B T)$ and $\beta = 1/(k_B T)$, where μ, k_B and T represent the chemical potential of the substrate, Boltzmann constant and the temperature, respectively. It has been reported that the image potential of grounded nano emitter is not sensitive to temperature,[45] in this article, T has been fixed at 300 K. With the electric force along the emitting path in hand, the potential barrier containing the image potential can be finally calculated by numerical integration of the electric force along the emitting path from the concerning emitting position to the remote place. We then remove the testing electron and calculate the potential barrier without the image potential. The difference between the former potential barrier and the latter potential barrier is caused by the image charges and is referred to as the image potential.

3. Results and discussion

Firstly, the potential barriers of Z-SWBNNTs under isolated and grounded conditions were investigated, as shown in Fig. 2. It is evident that the profile of potential barrier is relatively similar for the emitting points from the same side (i.e., sites I and II from N–H side, or sites III and IV from B–H side); however, noticeable differences in potential profiles exist among non-equivalent sides (e.g., site II from N–H side vs site III from B–H side). This phenomenon leads to the side-dependent characteristic of image potentials for Z-SWBNNT, which will be elaborated on in the following text. By taking the image potentials into account, the potential barrier (dashed line) exhibits a significant decrease compared to that without image potentials (solid line), consistent with the previous research.[44,45,69]

Figure 3 displays the image potentials of Z-SWBNNTs from different emitting points under isolated and grounded conditions. Only the image potentials from sites II and III are shown since the image potentials from the emitting points on the same side are almost the same [Figs. S1 and S2]. The image potential curves are found to be not sensitive to the diameter of Z-SWBNNT, as shown in Fig. 3(b). For short Z-SWBNNT (repeating units number $L < 3$), the image potentials are almost the same regardless of the emitting point under a given grounded condition [the topmost subgraph in Fig. 3(a)], while the image potentials (absolute value) in grounded condition are slightly larger than that in isolated condition [the topmost subgraph in Fig. 3(a)]. However, as the nanotube length increases, the image potentials for a given emitting point split into two different categories depending on the isolated and grounded conditions [the middle and the bottom subgraphs in Fig. 3(a)]. The absolute value of the image potential under grounded condition increases significantly with the increasing nanotube length, resulting in a more pronounced difference in image potential between grounded and isolated conditions. The reason why the image potential in grounded condition is greater than that in isolated condition can be attributed to the induced charge in grounded Z-SWBNNT, as shown in the insets of Fig. 3. It is obvious that the grounded Z-SWBNNT tends to be positively charged while the isolated Z-SWBNNT remains electrically neutral when the testing electron is in the vicinity of the tip of Z-SWBNNT. The former system leads to a stronger local electric field and lower potential barrier, and thus larger image potential. This conclusion is in agreement with the previous study for C_{60}.[45]

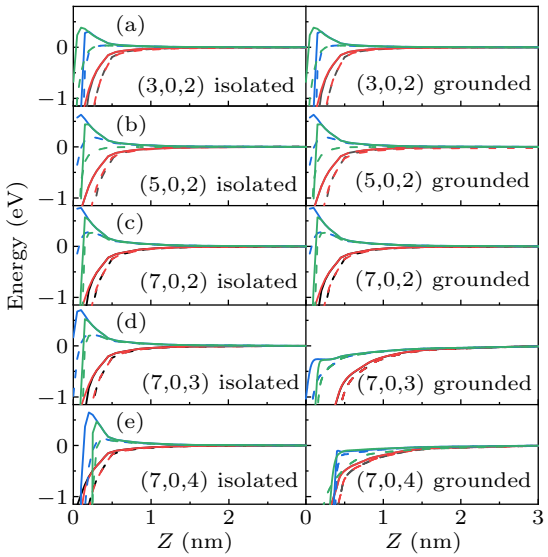


Fig. 2. Potential barrier distributions of (a) (3, 0, 2), (b) (5, 0, 2), (c) (7, 0, 2), (d) (7, 0, 3) and (e) (7, 0, 4) Z-SWBNNTs with (dashed lines) and without (solid lines) image potentials from emitting points I (black), II (red), III (blue) and IV (green) under isolated conditions (left panel) and grounded conditions (right panel).

To further explore the variation of image potential difference between isolated and grounded conditions as a function of the tube length, we analyze the Mulliken charge distribution on the four outermost atomic layers of Z-SWBNNTs under both isolated and grounded conditions, as shown in Fig. 4, where two positions of the testing electron (i.e., $z = 0.4$ nm and $z = 10$ nm) have been considered to investigate the sensitivity of induced charges to the distance between the testing electron and the emitter's tip. In the case of a larger distance ($z = 10$ nm), the Coulomb force of the testing electron can be negligible. In the case of $z = 0.4$ nm, however, the axial symmetries of charge distribution for both isolated and grounded conditions have been broken by the testing electron, and the axial symmetry breaking and field penetration at the tube tip are more significant for grounded conditions when $L > 3$ owing to the higher field enhancement factor caused by the higher

aspect ratio of longer Z-SWBNNT, leading to larger differences in the image potentials between isolated and grounded cases for longer tubes. Moreover, for a given grounded condition, the image potentials of long Z-SWBNNT exhibit significant termination-dependent characteristics, i.e., the image potential (absolute value) from the site III (i.e., H–B side) is much larger than that from the site II (i.e., H–N side) [see the bottom subgraph in Fig. 3(a)]. The termination-dependent characteristics has not been found in single-walled CNTs.[44] The difference in image potentials between the H–B side and the H–N side is found to increase with the increasing tube length. The reason should be attributed to the difference in electronegativity between N and B atoms, which can also be clearly seen in Mulliken charge distribution. As shown in Fig. 4, given that the electronegativity of the N atoms for the H–N side is larger than that of the B atoms for the H–B side, for the H–N side the outermost atomic layer H is positively charged and the second outermost atomic layer N is negatively charged; on the contrary, for the H–B side the outermost atomic layer H is nearly electrically neutral or even positively charged and the second (third) outermost atomic layer B(N) is positively (negatively) charged. The total number of positive charges and the effective distance between the negative charge center and the positive charge center are larger for the latter case. It has been predicted that the potential energy profile of the functional surface would be raised (reduced) by forming a plane of dipoles, whose direction points inwards (outwards) from the surface.[70,71] Therefore, a larger dipole moment pointing outward forms at the H–B side, resulting in more obvious image potentials. The dipole moment will increase on longer Z-SWBNNT owing to larger electrical polarization and induce charge accumulation at the edge of longer Z-SWBNNT, leading to increasingly significant edge-dependence characteristics of image potentials. This variation may be related to the complicated mechanism of charge transfer in nanotubes with different aspect ratios,[72,73] which demands further investigation.

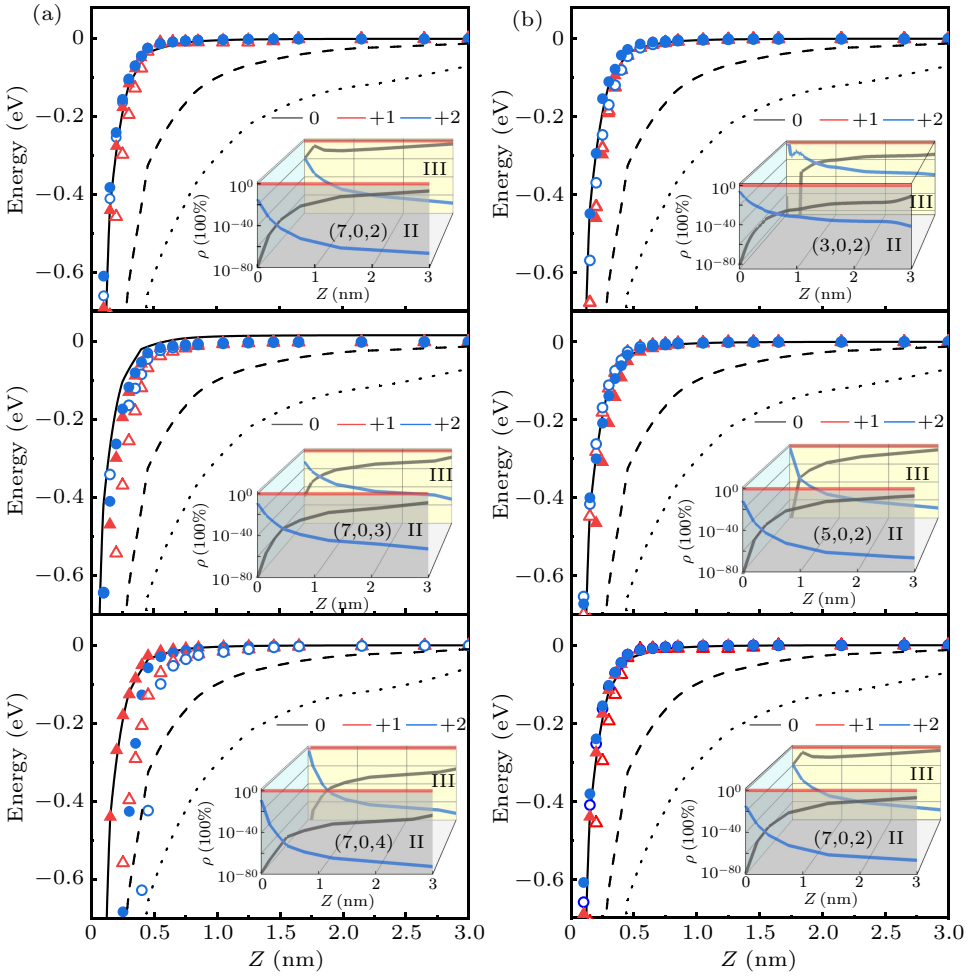


Fig. 3. Image potentials variation of isolated Z-SWBNNT from sites II (▲) and III (●) and grounded Z-SWBNNT from sites II (△), III (○) as a function of (a) tube length and (b) tube diameter. In (a) [(b)], the structural indices of Z-SWBNNTs from the top subgraph to the bottom subgraph are (7,0,2), (7,0,3) and (7,0,4) [(3,0,2), (5,0,2) and (7,0,2)], respectively. The image potentials of isolated (solid lines) and grounded (dashed lines) ideal metal spheres with the diameter equal to the corresponding Z-SWBNNT's diameter and the image potentials of the ideal metal plane (dotted lines) are shown for reference. Insets illustrate the probabilities of quantum states with two positive electron charges, one positive electron charge and zero positive electron charge (neutrality) as a function of distance from sites II and III for grounded Z-SWBNNT.

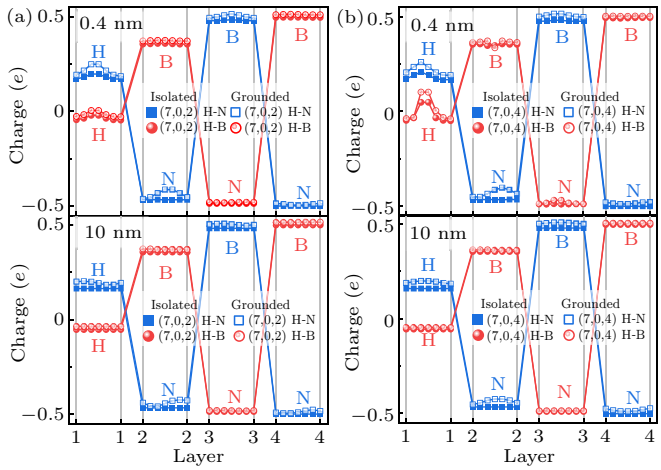


Fig. 4. (a) Mulliken charge distribution on the four outermost atomic layers of the H–N side (square) and H–B side (circle) of (7, 0, 2) Z-SWBNNT under isolated (solid) and grounded (hollow) condition when the testing electron locates at $z = 0.4$ nm (top panel) and $z = 10$ nm (bottom panel). (b) The same as (a) but for (7, 0, 4) Z-SWBNNT. The horizontal axis represents the number of atom layers. The seven atoms within the same layer are labeled by the same integer and spread out in the interval between two adjacent layer-indexes.

To provide insights into the difference between confined nano-system and macroscopic classical model, we further compare the results of Z-SWBNNTs with those of an ideal metal plane and isolated/grounded ideal metal sphere. The image potential of an ideal metal sphere with radius r is defined as the work done by the image electric field on the testing electron as it moves from z to a remote place.[41,42] When the ideal metal sphere is isolated, its image potential is given by

$$W_{\mathrm{id,i}}(z) = -\frac{e}{4\pi\varepsilon_0}\left\{\frac{r}{2[(z+r)^2 - r^2]} - \frac{r}{2(z+r)^2}\right\}. \quad (3)$$

When the ideal metal sphere is grounded, its image potential can be explicitly written as

$$W_{\mathrm{id,g}}(z) = -\frac{e}{4\pi\varepsilon_0}\frac{r}{2[(z+r)^2 - r^2]}. \quad (4)$$

When $r \to \infty$, we obtain the image potential of an ideal metal plane

$$W_{\mathrm{id,p}}(z) = -\frac{e}{4\pi\varepsilon_0}\frac{1}{4z}. \quad (5)$$

From Fig. 3, we find that the image potentials of both sides of short Z-SWBNNTs ($L \leq 3$) in isolated condition can be well approximated by an isolated ideal metallic sphere with the diameter equal to theirs. However, when Z-SWBNNTs are sufficiently long ($L \geq 4$), only the image potential from site II (i.e., the H–N side) in isolated condition can be accurately fitted by an isolated ideal metallic sphere model, while the image potentials from site II in grounded condition and site III (i.e., the H–B side) deviate significantly from the fitted curves of the ideal metallic sphere model. In addition, the image potentials of the classical ideal metal plane model adopted by Fowler–Nordheim theory are found to be no longer applicable in Z-SWBNNTs, which is in agreement with the previous theoretical research.[44,45] The above results indicate that the effect of microatomic structure on the image potentials of nano emitters cannot be ignored.

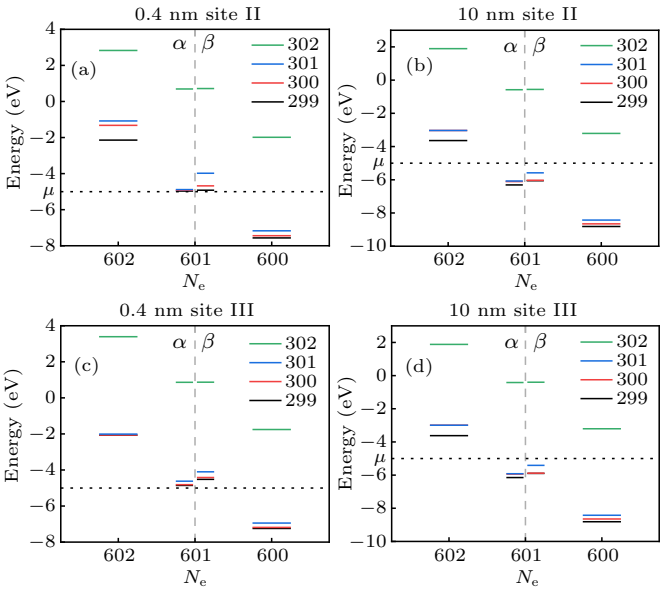


Fig. 5. Energy levels as a function of electron occupation in grounded (7, 0, 4) Z-SWBNNT from site II at a distance of (a) $z = 0.4$ nm and (b) $z = 10$ nm. The green, blue, red and black lines from top to bottom correspond to the 302nd, 301st, 300th and 299th energy levels, respectively. The dotted line represents the Fermi level. Only electron numbers ranging from 602 to 600 are displayed. The system is neutral when $N_e = 602$. When $N_e = 601$, the unrestricted Hartree–Fock calculation leads to spin-up (α) and spin-down (β) orbitals. (c)–(d) Same as (a)–(b) but from site III.

When the testing electron approaches the grounded Z-SWBNNT, the correlation between the testing electron and the electronic structure of Z-SWBNNT becomes significant. The Coulomb potential of the testing electron raises the energy levels of Z-SWBNNT. Subsequently, electrons tend to redistribute and escape from the Z-SWBNNT at the states with energies higher than the Fermi level. As shown in the insets of Fig. 3, the probability of neutral Z-SWBNNTs gradually decreases with decreasing z. The redistribution and leaving of electrons then make the energy levels lower. Figure 5 illustrates the variation of the energy levels as a function of the number of electrons in (7, 0, 4) Z-SWBNNT when $z = 0.4$ nm [Figs. 5(a) and 5(c)] and $z = 10$ nm [Figs. 5(b) and 5(d)]. When $N_e = 602$, the nanotube is neutral. All the energy levels move down as the total number of electrons in Z-SWBNNT decreases since the energy level distribution is closely related to the number of electrons. It can be clearly observed that the energy levels can be significantly affected by the emitting points from different sides of Z-SWBNNT at a close testing electron–tip distance [e.g., $z = 0.4$ nm, as shown in Figs. 5(a) and 5(c)], while the energy level distributions are nearly the same for emitting points from different sides of Z-SWBNNT when the testing electron locates at a remote place [e.g., $z = 10$ nm, as shown in Figs. 5(b) and 5(d)]. From Fig. 5, the lowest unoccupied molecular orbital of Z-SWBNNT with

one positive charge, i.e., the 301st orbital when $N_e = 601$, shifts downward from much higher than Fermi energy to near Fermi energy and will be occupied again. The probability of occupation is determined by the grand canonical ensembles, this phenomenon can explain why the quantum state of losing one electron is dominant.

We find that the overall profile of the image potential of A-SWBNNT differs from that of Z-SWBNNT. Given that the edges on both sides of A-SWBNNT are equivalent (see Fig. 1 and the relevant test in Figs. S3 and S4), only the potential energies and image potentials of one side will be discussed. The surface potential distribution curves of A-SWBNNTs under isolated and grounded conditions with different lengths and diameters are illustrated in Fig. 6. As the length of the nanotube increases, the decrease in the potential barrier of A-SWBNNT caused by the image potential is more significant.

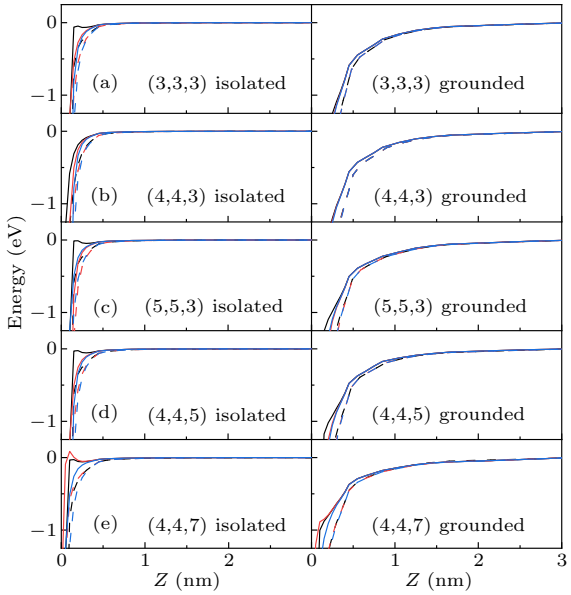


Fig. 6. (a) Potential barrier distributions for (3, 3, 3) A-SWBNNT under isolated condition (left panel) and grounded conditions (right panel). The dashed lines (solid lines) represent the potential barriers with (without) image potentials. The potentials from emitting points V, VI and VII are indicated by black, red and blue lines, respectively. (b)–(e) The same as (a) but for (4, 4, 3), (5, 5, 3), (4, 4, 5) and (4, 4, 7) A-SWBNNTs.

The variation of image potentials as a function of the length and diameter for A-SWBNNTs is summarized in Figs. 7(a) and 7(b), respectively. We only focus on the image potentials from emitting point V since the image potential of A-SWBNNT is insensitive to the emitting points (Figs. S4–S6), which is similar to single-walled CNTs and C_{60}.[44,45] The image potential of A-SWBNNT shows negligible diameter-dependent character [Fig. 7(b)], similar to that of Z-SWBNNT. The image potentials of isolated A-SWBNNTs are independent of the tube length [Fig. 7(a)]. The image potential of grounded A-SWBNNT is always larger than that of isolated A-SWBNNT, because the isolated (grounded) A-SWBNNT is neutral (positively charged) [see the insets of Fig. 7]. The positively charged grounded A-SWBNNT enhances the local electric field and lowers the potential profile, making the image potential larger. Compared to the case of Z-SWBNNT, the image potential difference between isolated and grounded conditions is found to increase with the increase of tube length slowly [Fig. 7(a)]. We performed Mulliken charge calculation on the four outermost atomic layers of the A-SWBNNT to analyze the above phenomenon, as shown in Fig. 8. For clarity, the edge hydrogen atom bonding to boron (nitrogen) is represented as H_B (H_N). Both boron and nitrogen atoms will exist in the same layer except for the outermost atomic layer [see Fig. 1(b)]. When the testing electron is close to the tip of the A-SWBNNT, the axial symmetry broken caused by the Coulomb force of the testing electron can also be observed, but the remarkable degree and the increase of axial symmetry broken as a function of tube length is not as significant as that of Z-SWBNNT [Fig. 8(a)]. Particularly, the degree of axial symmetry broken of isolated A-SWBNNT remains nearly unchanged. Figure 7 also illustrates the comparison of the image potentials between

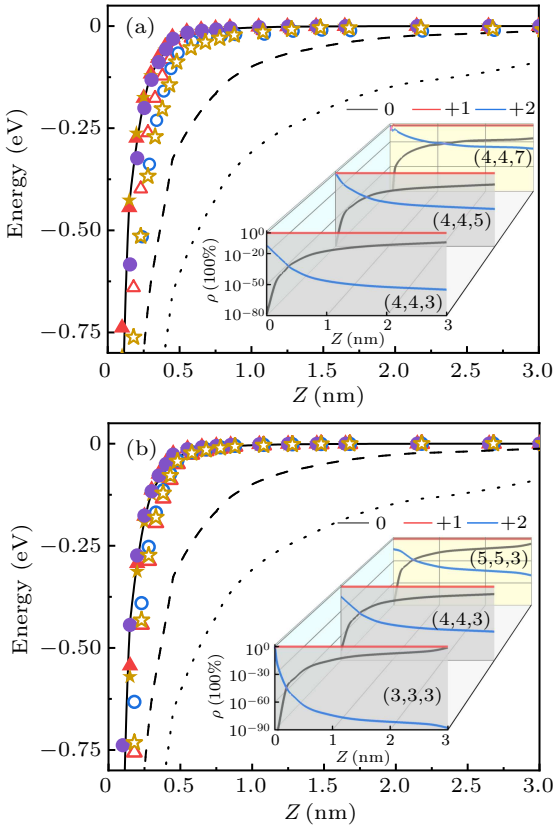


Fig. 7. (a) Image potentials of isolated (4, 4, 3) ▲, (4, 4, 5) ●, (4, 4, 7) ★ A-SWBNNT and grounded (4, 4, 3) △, (4, 4, 5) ◯, (4, 4, 7) ☆ A-SWBNNT. (b) Image potentials of isolated (3, 3, 3) ▲, (4, 4, 3) ●, (5, 5, 3) ★ A-SWBNNT and grounded (3, 3, 3) △, (4, 4, 3) ◯, (5, 5, 3) ☆ A-SWBNNT. The image potentials of isolated (solid line) and grounded (dashed line) ideal metal spheres with the diameter equal to that of (4, 4, 3) A-SWBNNT and the image potentials of the ideal metal plane (dotted lines) are also shown for comparison. Insets illustrate the probabilities of quantum states with two positive electron charges, one positive electron charge and zero positive electron charge (neutrality) as a function of distance under grounded conditions.

A-SWBNNTs and the ideal metal plane, an ideal metal sphere with the diameter equal to that of (4, 4, 3) A-SWBNNT. Only the image potential of isolated A-SWBNNT can be fitted with the isolated ideal metal sphere model with the diameter equal to that of A-SWBNNT, and this similarity can be explained by two reasons. (1) The axial symmetry broken on two equivalent terminations of isolated A-SWBNNT is nearly unchanged as the chirality indices (Fig. 8). (2) The tube diameters are comparable to tube lengths for the considered A-SWBNNTs (Table S1). The image potential of grounded A-SWBNNT is significantly different from that of a grounded ideal metal sphere. The image potential deviation between A-SWBNNT and the ideal metal plane can also be observed, indicating the microstructure of the nano emitter is important.

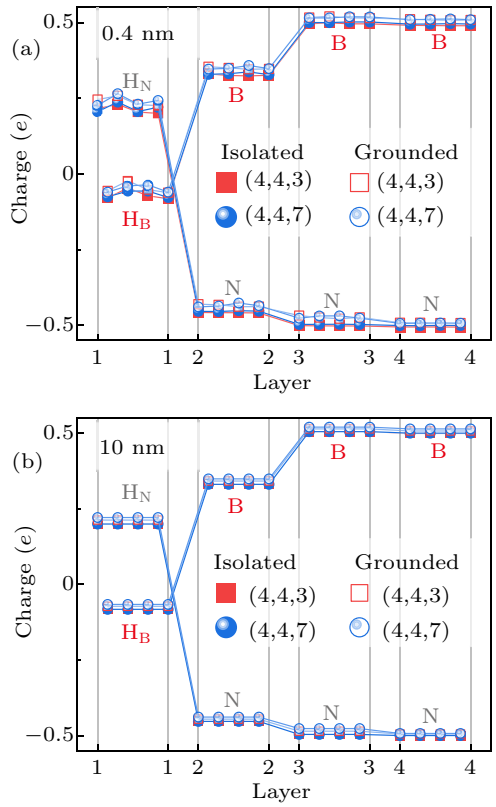


Fig. 8. (a) Mulliken charge distribution on the four outermost atomic layers of (4, 4, 3) (red square) and (4, 4, 7) (blue circle) A-SWBNNT under isolated (solid) and grounded (hollow) conditions when the testing electron locates at (a) $z = 0.4$ nm and (b) $z = 10$ nm, where H_B (H_N) represents the edge hydrogen atom bonding to boron (nitrogen). The horizontal axis represents the number of atom layers. The eight atoms within the same layer are labeled by the same integer and spread out in the interval between two adjacent layer indexes. Both boron and nitrogen atoms will exist in the same layer except for the outermost atomic layer.

To explore the correlation between the testing electron and the A-SWBNNT, the energy level distribution at the two positions of the testing electron near the surface of the (4, 4, 7) A-SWBNNT is shown in Fig. 9. When the system transitions from a neutral state ($N_e = 688$) to a positively charged state ($N_e < 688$), all the relevant energy levels shift downward. Moreover, similar to the results observed in Z-SWBNNT, the testing electron raises the energy levels of A-SWBNNT and leads to redistribution and departure of electrons within the system from the states with energy higher than the Fermi level. The lowest unoccupied molecular orbital (i.e., the 344th level) might drop below or near the Fermi level and become occupied again.

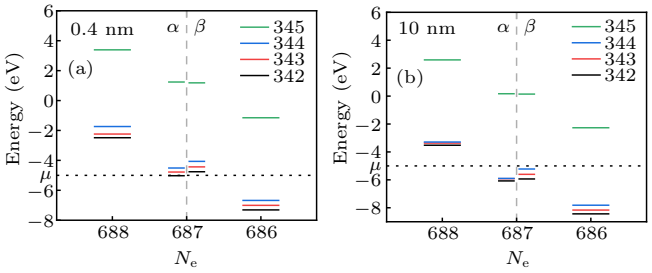


Fig. 9. Energy levels as a function of electron occupation in grounded (4, 4, 7) A-SWBNNT at a distance of (a) $z = 0.4$ nm and (b) $z = 10$ nm. The green, blue, red and black lines from top to bottom correspond to the 345th, 344th, 343rd and 342nd energy levels, respectively. The dotted line represents the Fermi level. Only electron numbers ranging from 686 to 688 are displayed. The system is neutral when $N_e = 688$. When $N_e = 687$, the unrestricted Hartree–Fock calculation leads to spin-up (α) and spin-down (β) orbitals.

4. Conclusions

We investigated the surface potential characteristics, image potentials, and charge distribution of zigzag and armchair SWBNNTs under isolated and grounded conditions using density functional theory. The probability of electronic occupancy was assumed to be determined by the grand canonical ensemble.

The image potentials for both A-SWBNNT and Z-SWBNNT are found to be insensitive to the tube diameters. Given the existence of the non-equivalent sides of Z-SWBNNT, i.e., H–B side and H–N side, the image potentials of Z-SWBNNTs exhibit significant termination-dependent characteristics. On the contrary, the image potentials of A-SWBNNTs are insensitive to the edges. The image potential difference between the isolated and grounded systems is small for short SWBNNT but rapidly increases with the increase of the tube length. Particularly, this increasing trend of Z-SWBNNT is more significant than that of A-SWBNNT. This phenomenon can be understood as the consequence of significant axial symmetry breaking of positive induced charge at the tip for the long grounded tube. We also compared the image potentials of SWBNNTs with those of ideal metal spheres and ideal metal plane. We found that only the image potentials of chirality structures with slight axial symmetry breaking of charge distribution (e.g., isolated A-SWBNNT, H–N side of isolated Z-SWBNNT) can be well modeled as that of an isolated ideal metal sphere of a size comparable to the tube diameter. The models of an ideal metal sphere and an ideal metal plane are invalid for grounded SWBNNTs and B–H side of

isolated Z-SWBNNTs, which can be attributed to the correlation between the discrete energy levels and the testing electron. We believe that this work illustrates practical and quantitative theoretical guidance to enhance the performance of field emission devices based on 1D nanostructures.

Acknowledgements

The authors acknowledge the financial support from the National Natural Science Foundation of China (Grant Nos. 12004083 and 51972069), the Science and Technology Projects in Guangzhou (Grant Nos. 202102020350 and 202102010470), the National Key R&D Program of China (Grant No. 2016YFB0200800), the Opening Project of Joint Laboratory for Planetary Science and Supercomputing (Grant No. CSYYGS-QT-2024-14), the Key-Area Research and Development Program of Guangdong Province (Grant No. 2019B030330001), the College Students Innovation and Entrepreneurship Training Program of Guangdong Province (Grant No. S202311078133), Key Discipline of Materials Science and Engineering, Bureau of Education of Guangzhou (Grant No. 202255464), the National Supercomputer Center in Guangzhou, the National Supercomputing Center in Chengdu, and the Network Center of Guangzhou University.

References

[1] Fowler R H and Nordheim L 1928 *Proc. R. Soc. Math. Phys. Eng. Sci.* **119** 173
[2] Charbonnier F 1996 *Appl. Surf. Sci.* **94–95** 26
[3] Dangwal-Pandey A, Müller G, Reschke D and Singer X 2009 *Phys. Rev. Spec. Top.-Accel. Beams* **12** 023501
[4] Crewe A V, Wall J D and Langmore J 1970 *Science* **168** 1338
[5] Dwivedi N, Neeraj Dwivedi, Neeraj Dwivedi, Dhand C, Dhand C, Carey J D, Anderson E C, Kumar R, Srivastava A K, Srivastava A K, Srivastava A K, Srivastava A K, Malik H K, Saifullah M S M, Kumar S, Kumar S, Lakshminarayanan R, Ramakrishna S, Bhatia C S and Danner A J 2021 *J. Mater. Chem. C* **9** 2620
[6] Li M, Shakoori M A, Wang R and Li H 2024 *Chin. Phys. Lett.* **41** 016302
[7] Sun L, Zhai F, Cao Z, Huang X, Guo C, Wang H and Ni Y 2023 *Chin. Phys. B* **32** 056301
[8] Huang C K, Ou Y, Bie Y Q, Zhao Q and Yu D 2011 *Appl. Phys. Lett.* **98** 263104
[9] Zhang Q, Zhang Q, Wang X and Wang Y 2020 *Inorg. Chem. Front.* **7** 1034
[10] Chang T H P, Kern D P, Muray L P and Muray L P 1992 *J. Vac. Sci. Technol. B* **10** 2743
[11] He H, She J C, She J, Huang Y, Deng S Z and Xu N 2012 *Nanoscale* **4** 2101
[12] Wang Y, Pan J A, Wu H and Talapin D V 2019 *ACS Nano* **13** 13917
[13] Colvin V L, Schlamp M C, A. P. Alivisatos, Alivisatos A P and Alivisatos A P 1994 *Nature* **370** 354
[14] Lin K, Xing J, Sarkar N, Quan L N, de Arquer F P G, Gong X, Lu J, Xie L Q, Xie L, Zhao W, Zhang D, Yan C, Li W, Liu X, Yan Lu, Lu Y, Kirman J, Sargent E H, Xiong J, Xiong Q and Wei Z 2018 *Nature* **562** 245
[15] Fakharuddin A, Gangishetty M K, Abdi-Jalebi M, Chin S H, Yusoff A B, Congreve D N, Tress W, Deschler F, Vasilopoulou M and Bolink H J 2022 *Nat. Electron* **5** 203
[16] Ahmad M, Sun H and Zhu J 2011 *ACS Appl. Mater. Interfaces* **3** 1299
[17] Grillo A, Barrat J, Barrat J, Galazka Z, Passacantando M, Ferrari A C, Giubileo F, Iemmo L, Luongo G, Urban F, Catherine Dubourdieu, Catherine Dubourdieu, Catherine Dubourdieu, Dubourdieu C and Di Bartolomeo A 2019 *Appl. Phys. Lett.* **114** 193101
[18] Yoon I T, Cho H D, Li M, Hang N T, Hojamberdiev M and Yang W 2020 *Appl. Surf. Sci.* **501** 144271
[19] Zhu Z Y, Sun Z, Zhou S D, Xu S, Li X, Li W, Wang L, Wong W Y, Yang W, Gao F and Chen S 2021 *J. Am. Ceram. Soc.*
[20] Li X, Lou C, Li W, Wang L, Gao F, Shao G, Wong W Y, Chen S and Yang W 2021 *ACS Appl. Mater. Interfaces* **13** 3062
[21] Chen J, Yang B, Lim Y D, Duan W, Zhao Y, Tay B K and Yan X 2020 *Nanotechnology* **31** 285701
[22] Grillo A, Passacantando M, Zak A, Pelella A and Di Bartolomeo A 2020 *Small* **16** 2002880
[23] Wu H, Shen S, Xu X, Qiao C, Chen X, Li J, Li W and Ou-Yang W 2020 *IEEE Trans. Electron Devices* **67** 5138
[24] Chernozatonskii L A, Kosakovskaya Z Ya, Gulyaev Yu V, Sinitsyn N I, Torgashov G V and Zakharchenko Yu F 1996 *J. Vac. Sci. Technol. B* **14** 2080
[25] Liu P, Liu P, Peng Liu, Jiang K, Wei Y, Liu X, Liu K, Liu L, Liang Liu, Fan S S and Fan S S 2010 *J. Vac. Sci. Technol. B* **28** 736
[26] Zhang H, Li D, Li D, Wurz P, Cheng Y, Cheng Y, Wang Y, Wang C, Sun J, Li G and Fausch R 2019 *Materials* **12** 2937
[27] Lingjie W, Zunxian Y, Jinyang L and Tai-liang G 2011 *J. Semicond.* **32** 123001
[28] Garry S, McCarthy E, Mosnier J P and McGlynn E 2014 *Nanotechnology* **25** 135604
[29] Chatterjee S, Kumar M, Pal A, Thakur I and Som T 2015 *J. Mater. Chem. C* **3** 6389
[30] Kim W J, Lee J S, Lee S M, Song K Y, Song K Y, Chu C N and Kim Y H 2011 *ACS Nano* **5** 429
[31] Lim Y D, Hu L, Xia X, Ali Z, Wang S, Tay B K, Aditya S and Miao J 2018 *Nanotechnology* **29** 015202
[32] Powers M J, Benjamin M C, Porter L M, Nemanich R J, Davis R F, Cuomo J J, Doll G L and Harris S J 1995 *Appl. Phys. Lett.* **67** 3912
[33] Chen Y, Zou J, Campbell S J and Le Caer G 2004 *Appl. Phys. Lett.* **84** 2430
[34] Cumings J and Zettl A 2004 *Solid State Commun.* **129** 661
[35] Song Y, Sun Y, Shin D H, Yun K N, Song Y H, Milne W I and Lee C J 2014 *Appl. Phys. Lett.* **104** 163102
[36] Yun K N, Sun Y, Han J S, Song Y H and Lee C J 2017 *ACS Appl. Mater. Interfaces* **9** 1562
[37] Karahka M and Kreuzer H J 2018 *Mater. Charact.* **146** 319
[38] Fursey G N 2003 *Appl. Surf. Sci.* **215** 113
[39] Blanco J M, Flores F and Pérez R 2006 *Prog. Surf. Sci.* **81** 403
[40] Yuasa K, Shimoi A, Ohba I and Oshima C 2002 *Surf. Sci.* **520** 18
[41] Edgcombe C J and Johansen A M 2003 *J. Vac. Sci. Technol. B* **21** 1519
[42] Edgcombe C J 2002 *Philos. Mag. B* **82** 1009
[43] Cutler P H, He J, Miskovsky N M, Sullivan T E and Weiss B L 1993 *J. Vac. Sci. Technol. B* **11** 387
[44] Wang W, Peng J, Chen G, Deng S, Xu N and Li Z 2008 *J. Appl. Phys.* **104** 034306
[45] Huang H, Li Z, Wang W and Chen G 2011 *J. Vac. Sci. Technol. B* **29** 021802
[46] Mayer A, Chung M S, Kumar N, Weiss B L, Miskovsky N M and Cutler P H 2006 *J. Vac. Sci. Technol. B* **24** 629
[47] Mayer A, Chung M S, Kumar N, Weiss B L, Miskovsky N M and Cutler P H 2007 *J. Vac. Sci. Technol. B* **25** 109
[48] Geis M W, Deneault S, Krohn K E, Marchant M, Lyszczarz T M and Cooke D L 2005 *Appl. Phys. Lett.* **87** 192115
[49] Silkin V M, Chulkov E V and Echenique P M 1999 *Phys. Rev. B* **60** 7820
[50] Silkin V M, Zhao J, Guinea F, Chulkov E V, Echenique P M and Petek H 2009 *Phys. Rev. B* **80** 121408
[51] Dhanabalan S C, Ponraj J S, Guo Z, Li S, Bao Q and Zhang H 2017 *Adv. Sci.* **4** 1600305
[52] Xiaozhi Bao, Bao X, Ou Q, Xu Z Q, Zhang Y, Bao Q and Zhang H 2018 *Adv. Mater. Technol.* **3** 1800072
[53] Sreedhar A, Hoai Ta Q T and Noh J 2023 *J. Ind. Eng. Chem.* **127** 1
[54] Muntwiler M, Zhu X and Zhu X Y 2008 *New J. Phys.* **10** 113018
[55] Schouteden K and Van Haesendonck C 2009 *Phys. Rev. Lett.* **103** 266805
[56] Damm A, Schubert K, Güdde J and Höfer U 2009 *Phys. Rev. B* **80** 205425

[57] Schubert K, Damm A, Eremeev S V, Sergey V. Eremeev, M. Marks, Marks M, Masahiro Shibuta, Shibuta M, Berthold W, Güdde J, Güdde J, Borisov A G, Tsirkin S S, Chulkov E V, Chulkov E V, Chulkov E V and Höfer U 2012 *Phys. Rev. B* **85** 205431
[58] Silkin V M, Lazić P, Došlić N, Petek H and Gumhalter B 2015 *Phys. Rev. B* **92** 155405
[59] David Nobis, Nobis D, Potenz M, Niesner D, Fauster Th and Fauster T 2013 *Phys. Rev. B* **88** 195435
[60] Craes F, Runte S, Klinkhammer J, Kralj M, Michely T and Busse C 2013 *Phys. Rev. Lett.* **111** 056804
[61] Borca B, Castenmiller C, Tsvetanova M, Sotthewes K, Rudenko A N, Zandvliet H J W and Zandvliet H J W 2020 *2D Mater.* **7** 035021
[62] Liu X, Wang L, Yakobson B I and Hersam M C 2020 *ACS Nano Lett.* **21** 1169
[63] Yang R and Sun M T 2023 *J. Mater. Chem. C* **11** 6834
[64] Barca G M J, Bertoni C, Carrington L, *et al.* 2020 *J. Chem. Phys.* **152** 154102
[65] Lee C T, Yang W T and Parr R G 1988 *Phys. Rev. B* **37** 785
[66] Becke A D 1993 *J. Chem. Phys.* **98** 5648
[67] Wang H, Yin Y, Yang X, Guo Y, Zhang Y, Yan H, Wang Y and Huai P 2022 *Chin. Phys. B* **31** 026102
[68] Wang J S, Zeng Y Y, Zheng Z Y, Zhang L, Wang B, Yang Y Q and Sun C Q 2023 *J. Phys. Chem. Lett.* **14** 8555
[69] Lang N D and Kohn W 1973 *Phys. Rev. B* **7** 3541
[70] Huang H M, Ding M Q, Zhang Y, Zhang S, Ling Y Y, Wang W L and Zhang S L 2023 *RSC Adv.* **13** 15148
[71] Mohammad Khazaei, Khazaei M, Khazaei M, Arai M, Sasaki T, Ranjbar A, Liang Y and Yunoki S 2015 *Phys. Rev. B* **92** 075411
[72] Tang N S, Yan X H and Ding J W 2005 *Acta Phys. Sin.* **54** 333 (in Chinese)
[73] Benavente Llorente V, Vázquez C I, Burgos M A, Baruzzi A M and Iglesias R A 2019 *Electrochimica Acta* **319** 990